Imaging Agents

International Edition: DOI: 10.1002/anie.201600234
German Edition: DOI: 10.1002/ange.201600234

Nanotexaphyrin: One-Pot Synthesis of a Manganese Texaphyrin-Phospholipid Nanoparticle for Magnetic Resonance Imaging

*Joseph M. Keca, Juan Chen, Marta Overchuk, Nidal Muhanna, Christina M. MacLaughlin, Cheng S. Jin, Warren D. Foltz, Jonathan C. Irish, and Gang Zheng**

Abstract: *The discovery and synthesis of novel multifunctional organic building blocks for nanoparticles is challenging. Texaphyrin macrocycles are capable and multifunctional chelators. However, they remain elusive as building blocks for nanoparticles because of the difficulty associated with synthesis of texaphyrin constructs capable of self-assembly. A novel manganese (Mn)-texaphyrin-phospholipid building block is described, along with its one-pot synthesis and self-assembly into a Mn-nanotexaphyrin. This nanoparticle possesses strong resilience to manganese dissociation, structural stability, in vivo bio-safety, and structure-dependent T_1 and T_2 relaxivities. Magnetic resonance imaging (MRI) contrast enhanced visualization of lymphatic drainage is demonstrated with respect to proximal lymph nodes on the head and neck VX-2 tumors of a rabbit. Synthesis of 17 additional metallo-texaphyrin building blocks suggests that this novel one-pot synthetic procedure for nanotexaphyrins may lead to a wide range of applications in the field of nanomedicines.*

Nanoparticles have been produced with a range of materials, such as lipids,[1] transition metals,[2] inorganic salts,[3] and even organic macrocycles.[4] The functions of these nanoparticles are usually unimodal, that is, one building block leads to one particular function. As a result, nanoparticles are commonly modified to include several building blocks, to create "multifunctional" agents. This perceived "all-in-one" approach does possess certain shortcomings, including a requirement for multistep syntheses and purification, complex toxicity studies for multiple components, and potentially heterogeneous formulations that pose a challenge for clinical translation.[5] In contrast, an approach may be used where a nanoparticle is composed of intrinsically multifunctional building blocks. This simplified approach lowers translation hurdles and allows for the discovery of new nanoscale properties, unseen with individual monomers. However, synthesizing such multifunctional building blocks, particularly those made of organic molecules, presents significant technical challenges. An example of organic multifunctional building blocks are porphyrin-lipids, which are capable of forming nanovesicles (porphysomes).[4] Porphysomes are applicable in photothermal therapy, photoacoustic imaging, activatable fluorescence imaging, and photodynamic therapy.[4] Additionally, they are capable of chelating ^{64}Cu in a stable fashion and consequently serve as a PET agent in vivo.[6] While these porphyrin building blocks possess attractive traits suitable for in vivo applications, their propensity for stable metal chelation is primarily limited to dications. This again stresses the need for the discovery of new, organic-based multifunctional building blocks that are synthetically attainable.

Texaphyrins are pentaaza Schiff base macrocycles that are related to porphyrins. In comparison with the 4-coordination pocket available in porphyrins, texaphyrins are capable of binding metals in an "expanded" 5-coordination pocket. With a demonstrable capacity to form 24 different stable 1:1 complexes with metal cations, applications of texaphyrins have been demonstrated in cancer therapy and imaging.[7] Absorbing strongly in the near-infrared range (700–900 nm), texaphyrins uniquely offer in vivo excitation. Additionally, texaphyrins exhibit selectivity to tumors and tolerable toxicity profiles in human subjects.[8] Moreover, changing the centrally coordinated metal in the texaphyrin core allows texaphyrin functionality to be tuned. Efforts have been made to incorporate texaphyrins into nanoparticles, such as the encapsulation of gadolinium-texaphyrin (GdTx) in nanoparticles for in vivo MRI,[9] and hyperthermia agents.[10] However, the use of texaphyrins as nanoparticle building blocks has not been reported. The discovery and synthesis of a texaphyrin-based building block capable of nano-assembly will enable the use of dozens of medically relevant metal ions in a single building block nanoparticle, thus unleashing the metal chelating power of texaphyrin for use in nanomedicines.

Our first venture into nano-assembly of a metallo-texaphyrin library started with the synthesis of a manganese Mn-texaphyrin-phospholipid building block. Paramagnetic Mn is a potent MRI contrast agent that causes strong reduction of both T_1 and T_2 relaxation time constants in tissue. Many chelation strategies have been developed to improve Mn delivery, including 1) in vivo stability, 2) bio-safety, and 3) contrast enhancement. Porphyrins have been used as a promising chelating macrocycle for Mn,[11] providing fairly stable complexes in vivo, while possessing efficacious contrast enhancement (mostly in the context of T_1).[12] The success of

[*] J. M. Keca, J. Chen, M. Overchuk, N. Muhanna, C. M. MacLaughlin, C. S. Jin, W. D. Foltz, J. C. Irish, Prof. Dr. G. Zheng
Princess Margaret Cancer Centre,
University Health Network (Canada)
E-mail: gang.zheng@uhnres.utoronto.ca
Homepage: http://sites.utoronto.ca/zhenglab
J. M. Keca, Prof. Dr. G. Zheng
Leslie Dan Faculty of Pharmacy, Department of Pharmaceutical Sciences, University of Toronto (Canada)
M. Overchuk, Prof. Dr. G. Zheng
Institute of Biomaterials and Biomedical Engineering, University of Toronto (Canada)
and
Department of Medical Biophysics, University of Toronto (Canada)

Supporting information for this article can be found under: http://dx.doi.org/10.1002/anie.201600234.

direct incorporation of Mn into the porphyrin lipid building blocks of porphysome nanoparticles imparted MRI sensitivity while improving photostability and providing nanostructure dissociation-driven signal enhancement. The larger architecture and stronger coordination (5-coordination state) of texaphyrin in comparison with traditional porphyrins (4-coordination state) could lead to more stable Mn-based chelation with new properties, such as improved stability and relaxivity.

Synthesis of texaphyrin-phospholipid failed repeatedly following previous reports for porphyrin-phospholipid syntheses by conjugation between an exocyclic porphyrin carboxylate and the hydroxy group of a lipid.[4] We developed a novel synthetic strategy by building a core C16-LysoPC conjugated *o*-phenylenediamine, which subsequently underwent a 1:1 Schiff base condensation with a tripyrrane dialdehyde. A five-carbon spacer is placed between the *o*-phenylenediamine and phospholipid, predictably aiding in favorable self-assembly interactions, such as van der Waals[13] and cation–alkane interactions.[14] The detailed synthetic methods for texaphyrin-phospholipid and subsequent Mn chelation will be reported elsewhere. Herein, we introduce the one-pot synthesis and self-assembly of Mn-texaphyrin-phospholipid. Mn was able to instantaneously chelate to texaphyrin-phospholipid upon addition of an organic base (such as triethylamine) at temperatures as low as −20 °C. Remarkably, the reaction was quantitative, requiring no additional purification after solvent removal. This high quantitative and efficient labelling protocol makes our texaphyrin-phospholipid conjugate suitable for radioisotope labelling, particularly ^{52}Mn (PET $t_{1/2} = 5.591$ d, $\beta+ = 29.6\,\%$, $E(\beta+)_{max} = 0.576$ MeV), enabling potential applications as a dual-modal PET/MRI imaging agent.[15] The UPLC-MS results (Figure 1) confirmed the texaphyrin-phospholipid structure, presenting the predicted masses for both free-base texaphyrin-phospholipid conjugate (*m*/*z* calcd for $C_{61}H_{95}N_6O_9P$ $[M]^+$ 1087.44, found 1088.00) and Mn-texaphyrin-phospholipid conjugate (*m*/*z* calcd for $C_{61}H_{90}MnN_6O_9P$ $[M]^+$ 1137.34, found 1136.8). The resultant Mn-texaphyrin-phospholipid, with an extinction coefficient of $\varepsilon_{451} = 23{,}400\,M^{-1}\,cm^{-1}$ and $\varepsilon_{743} = 10{,}600\,M^{-1}\,cm^{-1}$, subsequently self-assembled into the corresponding Mn-nanotexaphyrins (Figure 1). The formulation for these particles included 40 molar % cholesterol and 5 molar % 1,2-distearoyl-*sn*-glycero-3-phosphoethanolamine-*N*-[amino(polyethylene glycol)-2000] (DSPE-2KPEG), to improve in vivo pharmacokinetics.[16] These particles were monodisperse and were around 100 nm in size.

We evaluated Mn-nanotexaphyrin at a field strength of 7 T. The longitudinal (r_1) and transverse (r_2) relaxivities were determined by plotting the inverse relaxation time against the Mn-texaphyrin-phospholipid concentration (Figure 2). Intact Mn-nanotexaphyrins showed a dose-dependent increase in both T_1- and T_2-weighted images, where marked increases in positive (T_1) and negative (T_2) contrast enhancement were observed. A calculated r_1 of 0.81 $mM^{-1}s^{-1}$ was determined for intact Mn-nanotexaphyrins (Figure 2a). Geometric calculations for vesicles 100 nm in diameter, composed of phosphatidylcholine headgroups, indicate that there are roughly

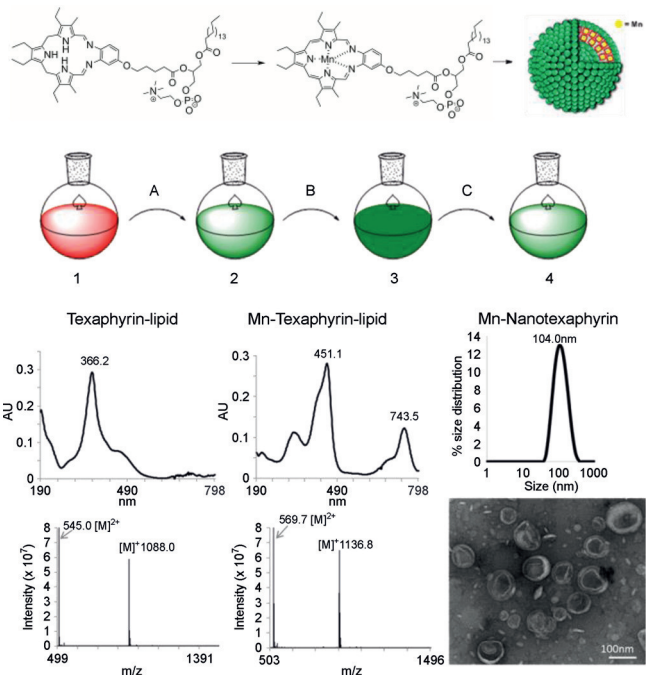

Figure 1. One-pot synthesis and self-assembly of Mn-nanotexaphyrin. The absorption spectra and corresponding mass spectra of texaphyrin-lipid and Mn-texaphyrin-lipid. Dynamic light scattering size and transmission electron microscopy (TEM) of Mn-nanotexaphyrin. Key: 1) texaphyrin-lipid, $Mn(OAc)_2$ in methanol; 2) Mn-texaphyrin-lipid; 3) lipid film; 4) Mn-nanotexaphyrin; A) NEt_3 at 0 °C; B) DSPE-2KPEG, cholesterol, evaporation; C) hydrated with PBS, self-assembly.

8×10^4 texaphyrin conjugates per nanotexaphyrin. Since each texaphyrin in our Mn-nanotexaphyrin constitutes a stable 1:1 porphyrin:metal chelation, this equates to each Mn-nanotexaphyrin carrying approximately 8×10^4 Mn^{II} ions (r_1 of $6.48 \times 10^4\,mM^{-1}s^{-1}$ per nanoparticle). We also investigated whether the supramolecular structure of Mn-nanotexaphyrins affected the longitudinal relaxivities by possible hindrance of the accessibility to water protons in the surrounding environment. After dissociating the Mn-nanotexaphyrins into individual monomers in PBS containing 0.5 % Triton X-100, a calculated r_1 of $0.99\,mM^{-1}s^{-1}$ was established, indicating a 22 % enhancement in comparison to the self-assembled construct. The high loading of Mn^{II} in each individual nanoparticle, coupled with enhanced delivery and selectivity to neoplastic tissues by the enhanced permeability and retention effect,[17] could offer advantages that are unattainable when individual monomers are used.

The transverse relaxivity properties of Mn-nanotexaphyrins were also evaluated and compared to the corresponding dissociated individual monomers. Intact Mn-nanotexaphyrins demonstrated an r_2 of $13.59\,mM^{-1}s^{-1}$ at 7 T. Following the same geometric calculations as previously mentioned, each Mn-nanotexaphyrin (100 nm in diameter) possesses an r_2 of $1.09 \times 10^6\,mM^{-1}s^{-1}$. Dissociating Mn-nanotexaphyrins into individual monomers lead to a calculated r_2 of $8.20\,mM^{-1}s^{-1}$, a 60 % decrease from that of intact Mn-nanotexaphyrins. This observation is in accordance with previous reports, which indicate that increasing particle size leads to increases in r_2.[18] The effect is presumably caused by an increase in the relative

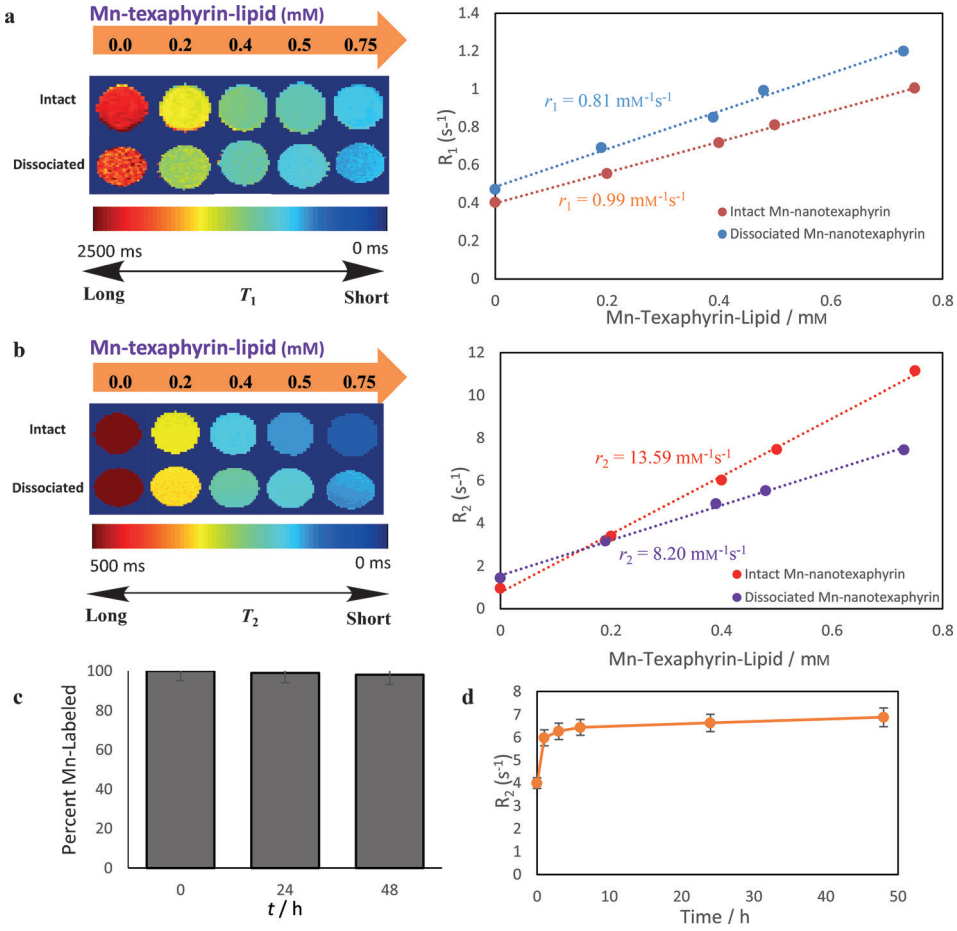

Figure 2. Solution-based MRI evaluation at high field strength (7 T) for both T_1 and T_2 relaxation. Quantitative a) T_1 and b) T_2 maps of Mn-nanotexaphyrin at varying concentrations in solution with corresponding plots of measured R_1 ($1/T_1$) and R_2 ($1/T_2$) values along with fitted linear regression lines and relaxivity values, respectively. c) Manganese chelation stability in serum (50% FBS) for 24 and 48 h ($n = 5$). d) Serum stability based on T_2 relaxation times.

saturation magnetization with increasing particle size, a correlation demonstrated in ferrites and iron-based nanoparticles.[19]

Mn-nanotexaphyrins maintained stable chelation to Mn in the presence of fetal bovine serum (FBS). Stability was evaluated by UPLC-MS, which allows a clear distinction to be made between free-base texaphyrin-phospholipid and Mn-texaphyrin-phospholipid by absorption spectroscopy and mass spectrometry. The stability of Mn-chelation to nanotexaphyrin was 99.5 ± 0.8% and 98.8 ± 0.8% after 24 and 48 h in 50% FBS, respectively, thus demonstrating the strong affinity of Mn for the texaphyrin macrocycle chelator (Figure 2c). Since Mn-coordination causes the "sp^3-texaphyrin" to become fully aromatic when chelating a metal ion, the thermodynamic favorability of aromaticity might contribute to the strong affinity of texaphyrin for Mn, and resilience to Mn dissociation. The structural stability of Mn-nanotexaphyrin in serum was evaluated by T_2-weighted imaging, where structural degradation can be observed in relation to a drop in R_2 values, as previously mentioned.

Mn-nanotexaphyrin in 50% FBS was shown to possess structural stability for up to 48 h, with no significant decrease in R_2 (Figure 2d). Instead, a slight initial increase in R_2 was observed in the presence of FBS (compared to the sample in PBS), indicating that Mn-nanotexaphyrin particles might form a protein corona, where a larger particle size induces an increase in the relative saturation magnetization.

Mn-nanotexaphyrin was evaluated for contrast enhancement in a lymphoscintigraphy procedure, which relies upon accumulation of the agent in sentinel lymph nodes (SLNs) using a head and neck VX-2 rabbit tumor with cervical lymph node metastases. Subcutaneous injection of Mn-nanotexaphyrin proximal to the tumor site was evaluated for its capacity to aid in visual enhancement of lymphatic drainage from the tumor site. T_1- and T_2-weighted imaging 2 h after injection showed increased visualization of lymphatic drainage from the tumor site to the adjacent metastatic lymph node (Figure 3). As a proof of concept, the images support the notion that Mn-nanotexaphyrin drains from the injection site towards the lymph node, thereby providing contrast enhancement in this area. Additionally, while still a proof of concept, these results highlight the potential utility of Mn-nanotexaphyrin for in vivo imaging as an MRI contrast agent for SLN biopsy procedures.

Subsequently, we evaluated the bio-safety of Mn-nanotexaphyrin in vivo, establishing whether this stability translated to in vivo tolerability and bio-safety. We performed a toxicity study to evaluate the potential for Mn-nanotexaphyrin acute toxicity effects (Supporting Information, Figure S1). Healthy female BALB/c mice ($n = 5$) were injected with a high dose (10 mg kg^{-1}) of Mn-nanotexaphyrin. After 24 h mice were sacrificed and the blood collected by cardiac puncture. Blood was collected from a control group of mice of the same age and gender, and was used as a reference for the tested parameters. We also demonstrated that treatment with a high dose of Mn-nanotexaphyrin does not affect the level of diagnostically significant liver enzymes. Counts of red blood cells and heme level did not change significantly, demonstrating unaffected physiological regulation of endogenous porphyrins. No change in white blood cell counts indicates that Mn-nanotexaphyrin is non-immunogenic in the acute phase. Major organs from the control and experimental groups of animals were harvested and sent for histopathology analysis

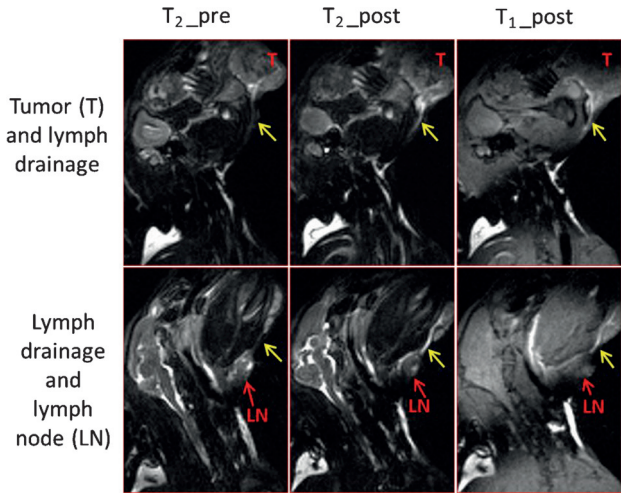

Figure 3. T_1- and T_2-weighted imaging of the tumor site (top) and lymph node (bottom) of a head and neck VX-2 rabbit tumor. Mn-nanotexaphyrin (8 mg mL^{-1}, 1.5 mL), was injected subcutaneously in the area surrounding the tumor. After 2 h, T_1- and T_2-weighted imaging was performed on a 7 T preclinical MRI system, showing enhanced visualization of lymphatic drainage from the tumor site to adjacent lymph nodes. Sagittal T_1- and T_2-weighted imaging of the head and neck area is shown for, T_2 (pre-injection), T_2 (post-injection), and T_1 (post-injection) of the tumor site (top) and the cervical metastatic LN (bottom). Clear signal enhancement was detected after injection of Mn-nanotexaphyrin demonstrated lymphatic drainage (yellow arrows).

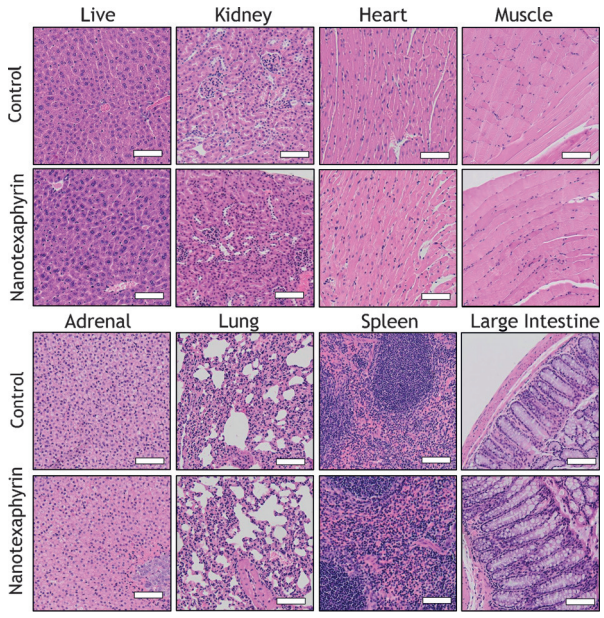

Figure 4. Representative haematoxylin and eosin stained sections of indicated mice organs 24 h after intravenous injection of 10 mg kg^{-1} Mn-nanotexaphyrin or PBS (control). Scale bar = 100 nm.

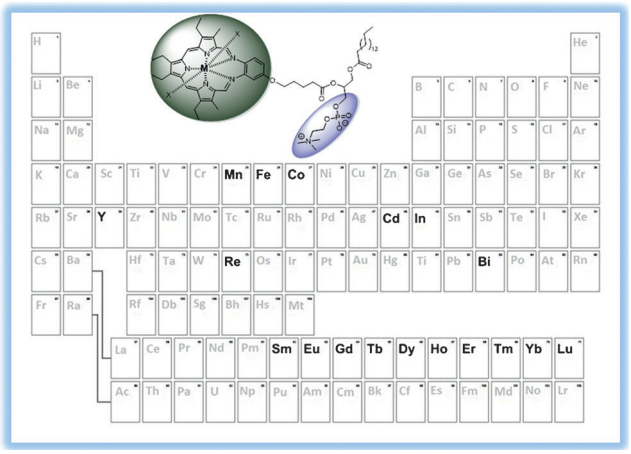

Figure 5. The texaphyrin-phospholipid conjugate chelation library. Elements demonstrated to have stable 1:1 chelation are displayed in bold.

(Figure 4), further demonstrating that Mn-nanotexaphyrin does not exhibit acute toxicity effects 24 h post-injection.

To broadly expand the purview of nanotexaphyrin utility, we further synthesized a library of 17 additional different metal-texaphyrin-phospholipid conjugates (detailed syntheses will be reported elsewhere). A large and diverse nanotexaphyrin library (Figure 5) was generated in this way, with each centrally coordinated metal-texaphyrin-phospholipid possessing its own unique, intrinsic properties, and potential applications in radiotherapy, radiosensitization, PET and SPECT imaging, MRI, photodynamic therapy, and fluorescence imaging. Moreover, these metal-texaphyrin-phospholipids can be combined to create mixed nanotexaphyrins with multifunctionality.

The formation of a new nanoparticle building block, and a proof of concept demonstration of the utility of a single nanotexaphyrin, highlights the potential of this nanotechnology. Promising results for the intrinsic r_1 and r_2 properties of Mn-nanotexaphyrin will prompt further evaluation and optimization of these contrast agents for in vivo imaging, and in so doing reveal the potential of these organic nanoparticle-based agents. Facile synthesis of Mn-nanotexaphyrin by one-pot self-assembly makes them suitable for future applications in ^{52}Mn PET imaging, expanding the utility of these agents beyond the field of MRI. This method offers new opportunities in nanomedicine, and addresses a need for innovative, organic-based, multifunctional building blocks, enabling the discovery of new nanoscale properties unseen with individual monomers.

Experimental Section

One-pot formation of Mn-nanotexaphyrin: Free-base texaphyrin-phospholipid conjugate (60 mg, 55.18 μmol) and $Mn(OAc)_2{\cdot}4H_2O$ (13.52 mg, 55.18 μmol) in anhydrous MeOH (10 mL) were added to a reaction vessel and cooled to 0 °C. Subsequently, triethylamine (76.71 μL, 551.75 μmol) was added, whereupon an instant color change from light red to deep green was observed, indicating instantaneous chelation of Mn. Cholesterol (14.83 mg, 40 mol %) and 1,2-distearoyl-*sn*-glycero-3-phosphoethanolamine-*N*-[amino(polyethylene glycol)-2000] (DSPE-2KPEG, 13.46 mg, 5 mol %) were introduced and the solvent removed under high vacuum, resulting in formation of a film. Films were rehydrated with PBS (30 mL), subjected to eight freeze-thaw cycles, and extruded with a 100 nm polycarbonate membrane at 75 °C. Mn-nanotexaphyrin size was determined with a Nanosizer ZS90 (Malvern Instruments). TEM images were collected using an FEI Technai 20 microscope with

200 kV accelerating voltage (and 150000x magnification). Samples were deposited on carbon-coated copper grids and incubated with 2% uranyl acetate stain to introduce image contrast. Fluorescence quenching of Mn-nanotexaphyrin was characterized using a Fluoromax fluorometer (Horiba Jobin Yvon). Mn-nanotexaphyrin solutions in PBS (intact particles), and PBS with 0.5% Triton-X100 (nanostructure disrupted samples), were excited at 460 nm and fluorescence emission spectra collected from 600–800 nm. The area under the emission peak was integrated and values from intact and dissociated nanoparticles compared.

Acknowledgements

The work was supported by funding from the Canadian Institutes for Health Research, Ontario Institute for Cancer Research, MaRS Innovation, Terry Fox Research Institute, Canada Foundation for Innovation, Prostate Cancer Canada, the Joey and Toby Tanenbaum/Brazilian Ball Chair in Prostate Cancer Research, and Princess Margaret Cancer Foundation.

Keywords: magnetic resonance imaging · metal chelation · nano-assembly · nanoparticles · texaphyrin

How to cite: *Angew. Chem. Int. Ed.* **2016**, *55*, 6187–6191
Angew. Chem. **2016**, *128*, 6295–6299

[1] T. Safra, F. Muggia, S. Jeffers, D. Tsao-Wei, S. Groshen, O. Lyass, R. Henderson, G. Berry, A. Gabizon, *Ann. Oncol.* **2000**, *11*, 1029–1033.
[2] M.-C. Daniel, D. Astruc, *Chem. Rev.* **2004**, *104*, 293–346.
[3] U. Banin, Y. Cao, D. Katz, O. Millo, *Nature* **1999**, *400*, 542–544.
[4] a) J. F. Lovell, C. S. Jin, E. Huynh, H. Jin, C. Kim, J. L. Rubinstein, W. C. Chan, W. Cao, L. V. Wang, G. Zheng, *Nat. Mater.* **2011**, *10*, 324–332; b) K. K. Ng, G. Zheng, *Chem. Rev.* **2015**, *115*, 11012–11042; c) E. Huynh, G. Zheng, *Nano Today* **2014**, *9*, 212–222.
[5] E. Huynh, G. Zheng, *Wiley Interdiscip. Rev. Nanomed. Nanobiotechnol.* **2013**, *5*, 250–265.
[6] T. W. Liu, T. D. MacDonald, J. Shi, B. C. Wilson, G. Zheng, *Angew. Chem. Int. Ed.* **2012**, *51*, 13128–13131; *Angew. Chem.* **2012**, *124*, 13305–13308.
[7] a) D. I. Rosenthal, P. Nurenberg, C. R. Becerra, E. P. Frenkel, D. P. Carbone, B. L. Lum, R. Miller, J. Engel, S. Young, D. Miles, *Clin. Cancer Res.* **1999**, *5*, 739–745; b) R. A. Miller, K. Woodburn, Q. Fan, M. F. Renschler, J. L. Sessler, J. A. Koutcher, *Int. J. Radiat. Oncol. Biol. Phys.* **1999**, *45*, 981–989; c) J. L. Sessler, N. A. Tvermoes, D. M. Guldi, T. D. Mody, W. E. Allen, *J. Phys. Chem. A* **1999**, *103*, 787–794; d) S. W. Young, F. Qing, A. Harriman, J. L. Sessler, W. C. Dow, T. D. Mody, G. W. Hemmi, Y. Hao, R. A. Miller, *Proc. Natl. Acad. Sci. USA* **1996**, *93*, 6610–6615; e) J. L. Sessler, M. R. Johnson, V. Lynch, *J. Org. Chem.* **1987**, *52*, 4394–4397; f) J. L. Sessler, T. D. Mody, G. W. Hemmi, V. Lynch, *Inorg. Chem.* **1993**, *32*, 3175–3187; g) J. L. Sessler, G. Hemmi, T. D. Mody, T. Murai, A. Burrell, S. W. Young, *Acc. Chem. Res.* **1994**, *27*, 43–50; h) S. Young, K. Woodburn, M. Wright, T. Mody, Q. Fan, J. Sessler, W. Dow, R. Miller, *Photochem. Photobiol.* **1996**, *63*, 892–897.
[8] J. L. Sessler, R. A. Miller, *Biochem. Pharmacol.* **2000**, *59*, 733–739.
[9] N. M. Barkey, C. Preihs, H. H. Cornnell, G. Martinez, A. Carie, J. Vagner, L. Xu, M. C. Lloyd, V. M. Lynch, V. J. Hruby, *J. Med. Chem.* **2013**, *56*, 6330–6338.
[10] D. Yoo, H. Jeong, C. Preihs, J. s. Choi, T. H. Shin, J. L. Sessler, J. Cheon, *Angew. Chem. Int. Ed.* **2012**, *51*, 12482–12485; *Angew. Chem.* **2012**, *124*, 12650–12653.
[11] a) L. J. Boucher, *J. Am. Chem. Soc.* **1968**, *90*, 6640–6645; b) N. C. Tam, P. Z. McVeigh, T. D. MacDonald, A. Farhadi, B. C. Wilson, G. Zheng, *Bioconjugate Chem.* **2012**, *23*, 1726–1730; c) T. D. MacDonald, T. W. Liu, G. Zheng, *Angew. Chem. Int. Ed.* **2014**, *53*, 6956–6959; *Angew. Chem.* **2014**, *126*, 7076–7079.
[12] a) H. L. M. Cheng, I. E. Haedicke, W. Cheng, J. Tchouala Nofiele, X. A. Zhang, *J. Magn. Reson. Imaging* **2014**, *40*, 1474–1480; b) W. Cheng, I. E. Haedicke, J. Nofiele, F. Martinez, K. Beera, T. J. Scholl, H.-L. M. Cheng, X.-a. Zhang, *J. Med. Chem.* **2014**, *57*, 516–520; c) Z. Zhang, R. He, K. Yan, Q.-N. Guo, Y.-G. Lu, X.-X. Wang, H. Lei, Z.-Y. Li, *Bioorg. Med. Chem. Lett.* **2009**, *19*, 6675–6678.
[13] A. Goursot, T. Mineva, R. Kevorkyants, D. Talbi, *J. Chem. Theory Comput.* **2007**, *3*, 755–763.
[14] J. R. Premkumar, G. N. Sastry, *J. Phys. Chem. A* **2014**, *118*, 11388–11398.
[15] G. J. Topping, P. Schaffer, C. Hoehr, T. J. Ruth, V. Sossi, *Med. Phys.* **2013**, *40*, 042502.
[16] J. M. Harris, R. B. Chess, *Nat. Rev. Drug Discovery* **2003**, *2*, 214–221.
[17] A. E. Hansen, A. L. Petersen, J. R. Henriksen, B. Boerresen, P. Rasmussen, D. R. Elema, P. M. Rosenschoeld, A. T. Kristensen, A. Kjær, T. L. Andresen, *ACS Nano* **2015**, *9*, 6985-6995..
[18] a) Y.-w. Jun, Y.-M. Huh, J.-s. Choi, J.-H. Lee, H.-T. Song, S. Kim, S. Kim, S. Yoon, K.-S. Kim, J.-S. Shin, *J. Am. Chem. Soc.* **2005**, *127*, 5732–5733; b) R. A. Brooks, F. Moiny, P. Gillis, *Magn. Reson. Med.* **2001**, *45*, 1014–1020.
[19] a) T. Sato, T. Iijima, M. Seki, N. Inagaki, *J. Magn. Magn. Mater.* **1987**, *65*, 252–256; b) H. Shokrollahi, *Mater. Sci. Eng. C* **2013**, *33*, 4485–4497; c) D. Pan, A. H. Schmieder, S. A. Wickline, G. M. Lanza, *Tetrahedron* **2011**, *67*, 8431–8444.

Received: January 8, 2016
Revised: March 1, 2016
Published online: April 13, 2016

